

1 **Compound Flooding in Convergent Estuaries:**
2 **Insights from an Analytical Model**

3
4
5 Ramin Familkhalili¹, Stefan A. Talke², and David A. Jay³

6 ¹Department of Civil and Environmental Engineering, Old Dominion University, Norfolk, VA, USA

7 ²Department of Civil and Environmental Engineering, California Polytechnic State University, San Luis Obispo, CA, USA

8 ³Department of Civil and Environmental Engineering, Portland State University, Portland, OR, USA

9
10
11
12
13
14 Correspondence to: Ramin Familkhalili (rfamilkh@odu.edu)

24 Key Points

- 25 • An idealized analytical model shows that deepening an estuarine channel reduces the
26 impacts of river flow on peak water level but increases the effects of storm tide.
- 27 • A friction number shows the competing effects of surge time scale, depth, and convergence
28 on water level amplitudes.
- 29 • Channel deepening changes the balance of fluvial and coastal flood risks and moves the
30 crossover between storm tide vs. fluvial-dominated flooding landward.

31 Abstract

32 We investigate here the effects of geometric properties (channel depth and cross-sectional
33 convergence length), storm surge characteristics, friction, and river flow on the spatial and
34 temporal variability of compound flooding along an idealized, meso-tidal coastal-plain estuary.
35 An analytical model is developed that includes exponentially convergent geometry, tidal forcing,
36 constant river flow, and a representation of storm surge as a combination of two sinusoidal waves.
37 Non-linear bed friction is treated using Chebyshev polynomials and trigonometric functions, and
38 a multi-segment approach is used to increase accuracy. Model results show that river discharge
39 increases the damping of surge amplitudes in an estuary, while increasing channel depth has the
40 opposite effect. Sensitivity studies indicate that the impact of river flow on peak water level
41 decreases as channel depth increases, while the influence of tide and surge increases in the
42 landward portion of an estuary. Moreover, model results show less surge damping in deeper
43 configurations and even amplification in some cases, while increased convergence length scale
44 increases damping of ~~damps~~ surge waves with ~~time scales~~ periods of 12 -72 h ~~along an estuary~~. For
45 every modeled scenario, there is a point where river discharge effects on water level outweigh
46 tide/surge effects. As a channel is deepened, this cross-over point moves progressively upstream.
47 Thus, channel deepening may alter flood risk spatially along an estuary and reduce the length of a
48 river-estuary, within which fluvial flooding is dominant.

49 Plain language summary

50 Storm surge, tides, and high river flow often combine to cause flooding in estuaries, a problem
51 known as compound flooding. In this study, we investigate these factors and how changes to
52 estuary and river geometry influence peak water levels. Our results show that surge waves become
53 larger when the depth of a shipping channel is increased, for example due to dredging or sea-level
54 rise. The same deepening, however, reduces the effect of river flow on peak water level. The result
55 is that the region over which river influence dominates the peak water level moves upstream as a
56 system becomes deeper. This change in the ‘cross-over location’ reduces the domain over which
57 river flooding is the dominant consideration. —This study offers an analytical framework for
58 reducing river-estuary flood risk by better understanding of how bathymetry, surge time scale, and

59 river discharge affect surge and tidal amplitudes, and therefore flood heights and inundation, in
60 these systems.

61 Keywords: Analytical model, Compound flooding, Estuary, Surge, Tide

62 1- Introduction

63 Understanding tidal, surge, and river flow dynamics, and how they combine and interact to produce
64 the maximum or total water level (TWL), is important for emergency planning and as an aspect of
65 wave dynamics. It is also a problem that is changing rapidly, as sea-level rises and systems are
66 altered by engineering. This contribution analyzes, therefore, the relative influence of river flow
67 and storm surge effects along the river-estuary continuum from a dynamical perspective that
68 enables us to assess the effects of non-linear interactions, geometry, and changing (time varying)
69 conditions.

70 Many low-lying coastal and riverine areas have been affected by combined coastal and riverine
71 floods over the last few decades (e.g., Jongman et al., 2012; Nicholls et al., 2007). In cases such
72 as Hurricane Harvey (Gulf of Mexico, August 2017), flooding was driven primarily by
73 precipitation and runoff (e.g., van Oldenborgh et al., 2017; Wang et al., 2018). Other flood events,
74 e.g., such as Hurricane Sandy, were forced by the combined effects of tide and storm surge, (i.e.,
75 by “storm tides” the sum of storm surge and tidal water level; (Orton et al., 2016). Some storm
76 events, like Hurricanes Irene and Irma, produce both coastal and inland flooding because both
77 storm surge and river flow produce elevated coastal water levels in a spatially varying pattern (e.g.,
78 Orton et al., 2012; Ralston et al., 2013; Talke et al., 2021). Accordingly, a flood ing event that is
79 influenced by both storm tide and precipitation run-off is ~~known as~~ a ‘compound flood’ (e.g.,
80 Zscheischler et al., 2018; Wahl et al., 2015). The relative timing of the coastal and fluvial forcing,
81 and the time scale over which water levels are elevated, matters in terms of impact (e.g., Zheng et
82 al., 2014). Storm surge flooding generally occurs first and for a shorter period (i.e., time scales of
83 hours to a day or two) than river flooding, which may last for weeks or even months, particularly
84 in regions with a large watershed and flat topography (e.g., Johnson et al., 2016, Wong et al.,
85 2014). The timing of storm surge relative to tidal high-water (Famalkhalili and Talke, 2016) or the
86 spring-neap tidal cycle also influences flood heights, even upstream of tidal influence (Helaire et
87 al., 2020).

88 The spatial variability of compound flooding is influenced by the geometry of an estuary region
89 and may change over time due to system alterations, including channel deepening, sea-level rise,
90 and wetland reclamation (Ralston et al., 2019; Helaire et al., 2019, 2020). Recent studies have
91 shown that human-caused changes to the geometry of estuaries affect the dynamics of long-waves
92 (see reviews by Talke and Jay, 2020, and Jay et al., 2021), with tidal range in some regions more
93 than doubling (e.g., Winterwerp et al., 2013). Similar effects are observed with storm surge; for
94 example, doubling the depth of the shipping channel in the Cape Fear Estuary was modeled to

95 increase the magnitude of a worst-case scenario storm surge in Wilmington (NC) ~~by from~~ $3.8 \pm$
96 0.25 m to 5.6 ± 0.6 m (Familkhalili and Talke, 2016). By contrast, depth increases ~~may~~ cause the
97 mean water level in tidal rivers to drop, due to decreased frictional effects (Jay et al., 2011; Helaire
98 et al., 2019); hence, flood risk in Albany (NY) has significantly dropped over the past 150 years,
99 despite a doubling of tide range and an increase in storm surge magnitudes (Ralston et al., 2019).
100 Closer to the coast, flood hazard within the same estuary markedly increased over the same time
101 period (e.g., Talke et al., 2014). Hence, ~~non-stationarity evolution of in~~ flood hazard can be
102 spatially variable, to an extent that is just beginning to be quantified.

103 ~~Here, an~~ idealized approach is used, which enables a large parameter space to be assessed and
104 the following two dynamical questions to be investigated:

- 105 a) What factors determine the region in which river flow effects or tide/surge effects dominate
106 the total water level?
- 107 b) How does the transition from coastal to fluvial dominance shift as geometry changes or as
108 properties of storm surge (e.g., time scale and magnitude) and river flow (magnitude)
109 change?

110 We combine a three-sinusoidal wave analytical model based on Jay (1991) with the multi-wave
111 and multi-segment approach of Giese and Jay (1989) (see Familkhalili et al., ~~(2020)~~ for details) to
112 quickly query a parameter space or relevant factors and provide insight into how factors such as
113 storm time scale and the relative magnitudes of different forcing factors influence the dynamics of
114 compound flooding.

116 2- Methods

117 Both, analytical solutions and numerical models are regularly used to explore the mechanism of
118 surge and tidal waves propagation along an estuary (see Talke and Jay, 2020 review). While
119 numerical models can simulate tidal wave propagation more accurately than analytical models
120 considering the measurements in a real system, numerical models are typically calibrated for an
121 existing bathymetric, meteorological, and boundary forcing configurations (e.g., Brandon et al.,
122 2014; Bertin et al., 2012; Orton et al., 2012). On the other hand, idealized numerical models with
123 simplified configurations can be used to develop sensitivity studies to investigate the effects of
124 changing hydrodynamic variables on surge and tidal wave interactions in a system (e.g., Shen and
125 Gong, 2009; Familkhalili and Talke, 2016), but a downside of these numerical approach is that
126 studying an entire parameter space is computationally expensive. In contrast, analytical models
127 rely on fundamental underlying physics and are transparent. Thus, they are good tools to explain
128 some of the factors (e.g., channel depth, convergence length, river discharge, and surge amplitude
129 and time scale changes) that alter flood levels in an estuary.

130 We apply an analytical approach to investigate the TWL caused by river discharge, tides, and surge
131 in an idealized estuary. Various forms of one-dimensional analytical solutions of tidal wave
132 propagation have long been used for idealized and real estuaries (e.g., Dronkers, 1964; Prandle
133 and Rahman, 1980; Jay, 1991; Friedrichs and Aubrey, 1994; Savenije, 1998; Lanzoni and
134 Seminara, 1998; Godin, 1999). More complex idealized tidal models investigate overtide
135 generation and evolution (e.g., Chernetsky et al., 2010), the effects of variable cross-section and
136 bottom slope (e.g., Savenije et al., 2008, Kästner et al., 2019), and the effects of multiple tidal
137 constituents and river discharge (Giese and Jay, 1989; Buschman et al., 2009). Other studies have
138 used a tidal model combined with regression analysis (e.g., Godin, 1999; Kukulka and Jay, 2003a)
139 to investigate river discharge effects. Such idealized models, by the parameter space analyzed, can
140 be used to obtain fundamental insights into how long waves in estuaries are affected by depth,
141 convergence, friction, and boundary forcing.

142 In our approach, we develop an analytical model which is driven by three sinusoidal constituents
143 and a constant river discharge. Our approach idealizes storm surge as the sum of two sinusoids,
144 and neglects factors, such as the potential role of wetlands and the floodplain, in order to gain
145 insight into some of the important, along-channel factors that govern the system response to a
146 compound event. Similarly, we neglect processes such as Coriolis acceleration, wind waves, and
147 gravity waves, and focus on the specific case of an incident long-wave that propagates from the
148 coast in the landward direction and is eventually completely damped out. Though a reflected wave
149 is produced by convergent geometry in analytical models (Jay, 1991), we neglect the partial
150 reflections caused by depth and width changes, and do not consider the case of a reflective
151 upstream boundary. Such factors are important for tidal changes in many estuaries, particular
152 locations that are near resonance such as the Ems (see Ensing et al., 2015) or near where total
153 reflections occur (see Ralston et al., 2019). ~~Moreover~~, we simplify our approach by considering
154 only constant river flow conditions, a valid approximation for situations in which the time scale of
155 a river flood event is much longer than a storm surge. These simplifications enable a solution that
156 is much faster than numerical models and enables a tractable sensitivity study of storm surge and
157 river flow effects on water levels for different depths, convergence, and boundary conditions.

158 **2-1- Analytical model**

159 We use an idealized one-dimensional analytical model developed by Familkhalili et al., (2020) to
160 investigate how combinations of tides, storm surge, and river flow affect water levels in an estuary.
161 In this model, storm surge is approximated as the sum of a primary and a secondary sinusoidal
162 wave. A third sinusoidal frequency is reserved for the M_2 tidal constituent. ~~Hence, t~~ The resulting
163 model is conceptually similar to the multi-tide constituent model developed by Giese and Jay
164 (1989) and the three-wave model of Buschman et al., (2009), with the distinction that two of the
165 waves are based on the amplitude and timescales of meteorologically induced storm surge rather
166 than an astronomical tide with a known frequency. Also, the Giese and Jay (1989) model used the
167 dynamical analysis of Dronkers (1964), that does not correctly include convergence effects,

168 whereas our model follows the Jay (1991) treatment that includes friction, convergence, and river
 169 inflow.

170 One-dimensional long wave propagation along an idealized, funnel-shaped estuary is described by
 171 the cross-sectionally integrated equations of mass and momentum conservation (e.g., Jay, 1991;
 172 Kukulka and Jay, 2003a; Familkhalili et al., 2020):

$$173 \quad \frac{\partial Q}{\partial t} + \frac{\partial}{\partial x} \left(\frac{Q^2}{A} \right) + gA \frac{\partial \xi}{\partial x} + bK\mathcal{F} = 0 \quad (1)$$

$$174 \quad \frac{\partial Q}{\partial x} + b \frac{\partial \xi}{\partial t} = 0 \quad (2)$$

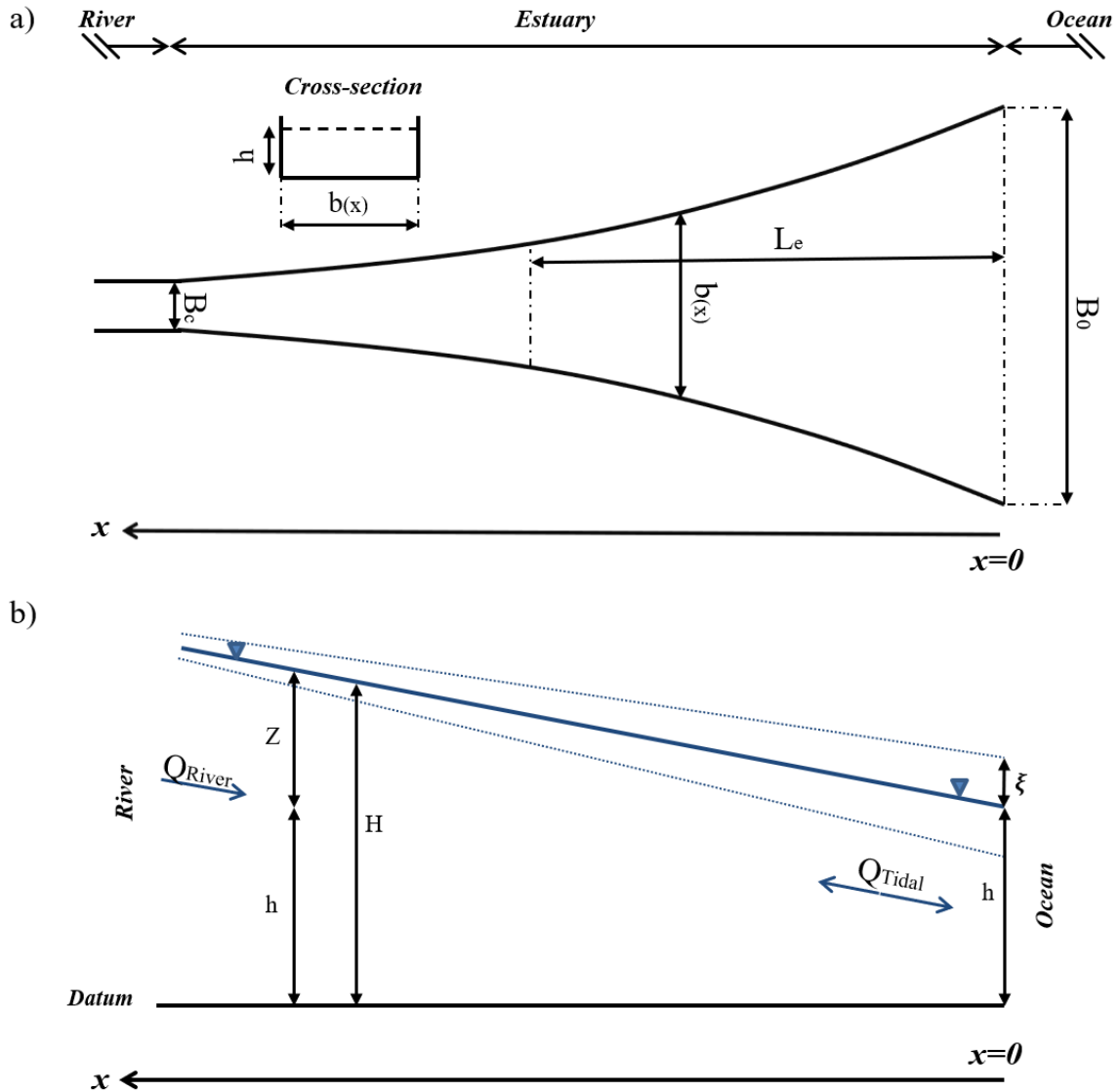
175 where Q is cross-sectionally integrated flow ($m^3 s^{-1}$) and is the summation of the river and tidal
 176 transports ($Q_R + Q_T$), t is time (s), x is the longitudinal coordinate measured in landward
 177 direction (m) (see Fig. 1a), b is width (m), g is the acceleration due to gravity ($9.81 ms^{-2}$), A is
 178 channel cross-sectional area (m^2), ξ is tidal ~~water level elevation amplitude~~ (m), $K\mathcal{F}$ is the bed
 179 stress divided by water density ($m^2 s^{-2}$) ($\frac{\tau}{\rho} = C_d |u|u$), C_d is a dimensionless drag coefficient, and
 180 $u = Q/A$ is the velocity (ms^{-1}). The absolute value of u is assigned to preserve the directionality
 181 of stress. For simplicity, depth is assumed constant and channel width is allowed to vary
 182 exponentially with respect to the longitudinal coordinate x (i.e., $b_{(x)} = B_c + (B_0 - B_c)e^{(-\frac{x}{L_e})}$, see
 183 Fig. 1a), where B_0 is the width at the estuary mouth (m) and B_c is the constant upstream river width
 184 (m) and L_e is the convergence length scale (m) that is the length over which the width decreases
 185 by a factor of e . Following Familkhalili et al (2020), we set $B_0=5$ km and assume that the estuary
 186 section of the model domain is 1.5 times the convergence length which determine a constant river
 187 width of ~ 1100 m. The constant depth channel is routed upstream for 100 km, to enable the tide
 188 wave to dissipate and prevent reflection off an upstream boundary. The tidal amplitude to depth
 189 ratio ($\frac{\xi}{h}$) is assumed small, and river flow (Q_R) is held constant (e.g., Kukulka and Jay, 2003a;
 190 Familkhalili et al., 2020). Applying these assumptions and combining Eq. (1) and (2) yields the
 191 following differential equation:

$$192 \quad \frac{\partial^2 Q_T}{\partial x^2} - \frac{1}{b} \frac{\partial b}{\partial x} \frac{\partial Q_T}{\partial x} - 2 \frac{1}{gh} U_R \frac{\partial^2 Q_T}{\partial x \partial t} + 2 \frac{1}{gh} U_R \frac{1}{A} \frac{\partial A}{\partial x} \frac{\partial Q_T}{\partial t} - \frac{1}{gh} \frac{\partial^2 Q_T}{\partial t^2} - \frac{b}{gh} \frac{\partial K\mathcal{F}}{\partial t} = 0 \quad (3)$$

193 We linearize the frictional term ($K\mathcal{F} = C_d |u|u$) using Chebyshev polynomials (Dronkers, 1964)
 194 to approximate the frictional term, $u|u|$. Following Godin (1991, 1999), only the first and third
 195 order terms of the dimensionless velocity are retained, yielding:

$$196 \quad \frac{u|u|}{U_{(x)}^2} \approx Au' + Bu'^3 \quad (4)$$

197 where $A = \frac{16}{15\pi}$, $B = \frac{32}{15\pi}$, $U(x)$ is a function of x and is the maximum value of the total current
 198 ($U_R + U_T$), where U_R and U_T are maximum river and tidal velocity, respectively, and is a
 199 function of x , and u' is a non-dimensionalized velocity defined as $\frac{u}{|U(x)|}$ (Doodson, 1956; Godin,
 200 1991). See Familkhalili et al., (2020) for additional details.



201
 202 Figure 1. (a) Idealized bathymetry and plan view of the conceptual model and (b) definition of the water surface
 203 slope, modified from Kukulka and Jay (2003b). Along channel direction x is upstream with $x=0$ at the ocean. The
 204 convergent section of the model domain is 1.5 times the convergence length and the river channel at the left-hand
 205 side extends an additional 100 km to enable tidal and surge constituents to damp out. See Appendix for a description
 206 of parameters.

207 The sectionally and vertically averaged velocity term in Eq. (3) ($u = Q/A$) is decomposed into three
 208 sinusoidal wave components and a constant river discharge:

$$u = -u_r + \sum_{i=1}^3 u_i \cos(\omega_i t + \phi_i) \quad (5)$$

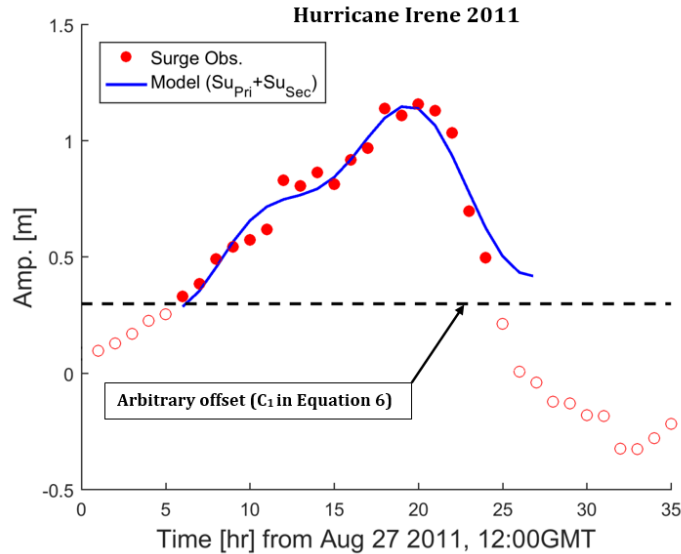
209 where u_r is the river flow velocity ($m s^{-1}$), and u_i , ω_i , ϕ_i are velocity amplitudes, frequencies,
 210 and phases, respectively. Although river discharge is not constant on ~~the seasonal or time scale of~~
 211 weather systems (5-7 day) ~~time scales and seasonal time scales~~, we assume for simplicity that the
 212 change over a tidal cycle or storm surge wave (generally <2 day time-scale) can be neglected. This
 213 limits our analysis to river systems with a long-response time, i.e., ~~it our approach~~ is inappropriate
 214 for short, steep, flashy systems with flood time scales < 2 days.

215 We use a multi-segment approach (Dronkers, 1964), to divide the model domain into N segments,
 216 each has a constant depth and exponentially varying width. This approach produces a system of
 217 $2N$ linear equations with $2(N-1)$ internal, one seaward, and one landward boundary conditions. The
 218 landward of our analytical model is forced by a no-reflection condition with constant discharge
 219 and the seaward boundary (see Fig. 1) is forced by 3 sinusoidal water level signals. One of the sine
 220 waves represents the main semidiurnal tidal constituent, and two of the sine waves represent the
 221 elevated water level of the surge signal in terms of primary and secondary components, denoted
 222 by the *Pri* and *Sec* subscripts (Famalkhalili et al., 2020):

$$Surge = \underbrace{A_{Pri} \cos(\omega_{Pri} t + \phi_{Pri})}_{Surge_{Pri}} + \underbrace{A_{Sec} \cos(\omega_{Sec} t + \phi_{Sec})}_{Surge_{Sec}} + \underbrace{C_1}_{Constant} \quad (6)$$

223 where A is the amplitude, ω is the frequency, ϕ is the phase, and C_1 is an arbitrary offset. For
 224 simplicity, the surge is treated as a free wave within the model domain, i.e., we neglect the effect
 225 of wind stress and any locally generated component of surge.

226 An example fit using two sinusoidal waves to a ~~hurricane~~-surge ~~caused by Hurricane Irene (August~~
 227 ~~2011)~~ is shown in Fig. 2. The surge signal is calculated by subtracting predicted tide from observed
 228 water level at Lewes, DE (NOAA Station ID: 8557380) ~~and is caused by Hurricane Irene (August~~
 229 ~~2011)~~. Fitting two sinusoidal waves approximates the surge signal with correlation of $R^2=0.95$ and
 230 root-mean-square-error of 0.05 m (Fig. 2). The fit is valid for the time period that the surge remains
 231 above the dashed line.



232

233 Figure 2. An example of decomposing surge into two sinusoidal waves. The red circles represent surge and are
 234 calculated by subtracting predicted tide from measured water level during Hurricane Irene (2011) at Lewes, DE
 235 (NOAA Station ID: 8557380). The blue line is the model fit that is the sum of Su_{pri} and Su_{sec} and black dashed line
 236 shows the threshold constant C_1 , per Eq. (6).

237 Typical amplitudes, frequencies, and phases of the two component surge waves are determined by
 238 fitting two sinusoids to 354 storm surge events from Lewes, DE. These results are used to define
 239 the parameter space that we investigate (Sect. 4) and are typical of coastal storm surge
 240 characteristics on the mid-Atlantic Bight. Only significant events, with surges larger than 0.5 m,
 241 are fit. The largest resulting primary surge wave amplitude was about 1.1 m, larger than but of the
 242 same order as the main tidal constituent ($M_2 = 0.6$ m). The statistically significant fits ($R^2 = 0.91$)
 243 have average primary and secondary surge periods of ~ 29 and ~ 16 h, respectively.

244 2-2- River discharge effects on water surface slope

245 The presence of river discharge (Qu_R) and tidal ~~velocities-transport~~ (Qu_T) causes stronger ebb
 246 currents ($|Q_T| + |Q_R|$) and weaker flood currents ($|Q_T| - |Q_R|$). The resulting non-linear
 247 interaction and increased friction typically reduces the tidal range, ~~delays arrival shifts the timing~~
 248 of high and low water (e.g., Godin, 1985; Hoitink and Jay, 2016), and generates tidal distortion
 249 (asymmetry), ~~expressed as the presence of overtides, e.g., M_4 in semidiurnal dominant systems~~
 250 (Parker, 1991). The increased frictional ~~effects~~ also influences subtidal water levels, producing a
 251 larger river slope (Kukulka and Jay, 2003b; Buschman et al., 2009; ~~Kästner et al., 2019-Talke et~~
 252 ~~al., 2021~~). However, typical coastal plain systems in the western Atlantic have low river flow
 253 relative to tidal ~~discharge-transport amplitudes~~. For example, the $\sim 200 \text{ m}^3 \text{ s}^{-1}$ average annual
 254 ~~river~~ discharge of the Saint Johns River Estuary, Florida, is about 5 % of total discharge (river +
 255 tides) (Talke et al., 2021). Similarly, the Delaware River Estuary has mean and median river flows
 256 at Trenton, NJ of $\sim 340 \text{ m}^3 \text{ s}^{-1}$ and $285 \text{ m}^3 \text{ s}^{-1}$, respectively, small compared to tidal flow of $\sim 23 \times 10^4$

257 $m^3 s^{-1}$ at the mouth (USGS, 2018; Munchow et al., 1992). The Cape Fear River has an average
 258 river discharge of $268 m^3 s^{-1}$ (Famalkhalili and Talke, 2016), which is less than 5 % of total
 259 averaged ebb-tidal flow (Olsen, 2012).

260 River flow alters the water surface slope, and this behavior influences the spatial distribution of
 261 total water level (e.g., Fig. 1b). Here, we use the tidally averaged one-dimensional equation of
 262 motion to investigate water level gradients, following Kukulka and Jay (2003b) and Godin (1999).
 263 For simplicity, ~~we~~ the component of mean water level caused by the tidal Stokes drift is
 264 ~~considered~~ neglected. The parameter h is the mean depth of water (m), ξ is the tidal ~~amplitude~~
 265 amplitude (m) (small compared to depth), Z is the perturbation in the water surface elevation due
 266 to river discharge Q_R , and is assumed to be much smaller than h . In this study, normalized river
 267 flow velocity (applied at the upstream boundary) is parameterized as the ratio of the river velocity
 268 magnitude to the magnitude of the major tidal component velocity at the ocean boundary (i.e., $\frac{|u_r|}{|u_{D_2}|}$
 269 or θ hereafter). To evaluate the effect of elevated river discharge, we consider a river flow ratio
 270 of 0 to 1. The ratio of $\theta = 1$ represents a case in which river and tidal flows are comparable, and
 271 thus is outside the zone of our assumptions; however, comparisons with numerical model results
 272 suggest that results below this ratio are reasonable (see Sect. 3.1). Therefore, we assess both low-
 273 flow conditions and conditions in which the river flow is comparable to tidal discharge.

274 Previous studies (e.g., Ralston et al., 2019; Helaire et al., 2019; Talke et al., 2021) showed that
 275 reduced friction due to increased channel depth can alter the tidally averaged water level gradient
 276 ($\frac{\partial Z}{\partial x}$, Fig. 1b). This water level gradient ~~R~~ (river slope) can be determined from the one-dimensional
 277 equation of motion (Godin, 1999):

$$\underbrace{\frac{1}{g} \frac{\partial \bar{u}}{\partial t}}_{\text{Local acceleration}} + \underbrace{\frac{\bar{u}}{g} \frac{\partial \bar{u}}{\partial x}}_{\text{Convective acceleration}} = - \underbrace{\frac{\partial H}{\partial x}}_{\text{Pressure gradient}} - \underbrace{\frac{\bar{u}|\bar{u}|}{C_h^2(h + \xi)}}_{\text{Friction}} \quad (7)$$

278 where \bar{u} is tidally averaged value of the current at x (ms^{-1}), g is the acceleration due to gravity
 279 (ms^{-2}), C_h is Chézy coefficient ($m^{1/2}s^{-1}$), and h is the mean depth of water (m). Scaling the
 280 terms in Eq. (7) using values typically found in estuaries (e.g., Godin and Martinez, 1994; Kukulka
 281 and Jay, 2003b, Buschman et al., 2009) shows that zero-order balance is between the pressure
 282 gradient and the friction term, so that the entire left-hand side of Eq. (7) can be neglected. We
 283 adopt this simplification for our idealized geometry, but note that as small, though the convective
 284 term may be locally important in real systems with complex geometry (e.g., Helaire et al., 2019).
 285 ~~Since~~ The cross-sectional area in our model varies smoothly (exponentially) over a large length
 286 scale; thus, our approach neglects convective effects in the mean momentum balance. We also
 287 neglect the riverbed slope, which is typically small in estuaries, particularly in modern dredged
 288 systems (see e.g., Talke et al., 2021). Within the upstream reaches of tidal rivers, the bed slope
 289 often increases and is important dynamically (Kästner et al., 2019); therefore, we restrict our

290 analysis and interpretation to estuarine reaches. As before, we assume that the tidal amplitude to
 291 depth ratio ($\frac{\xi}{h}$) is small. Given these assumptions, we simplify Eq. (7) to the following balance
 292 (Godin and Martinez, 1994):

$$\frac{\partial \bar{H}}{\partial x} = -\frac{\bar{u}|\bar{u}|}{C_h^2 \bar{h}} \quad (8)$$

293 where \bar{H} is total water elevation and \bar{h} is the mean water level (the overbar denotes the tidally
 294 averaged value). The low-frequency momentum Eq. (8) shows that the surface slope is defined by
 295 the bed stress term. ~~Considering the first and third terms in~~Using Eq. (4), we use a polynomial
 296 form of the bed stress (i.e., $\bar{u}|\bar{u}|$) to solve ~~the equation~~Eq. (8) (see Sect. 2.1).

297 3- Model validation

298 The above tide-surge analytical model has previously been compared against two one-constituent
 299 analytical models (the Toffolon and Savenije, 2011 and Jay, 1991 tidal solutions) and idealized
 300 Delft-3D numerical model results for situations without river flow (see Familkhalili et al., 2020).
 301 Results showed that our analytical model is capable of capturing tidal wave amplitudes that are in
 302 good agreement with numerical models results. ~~Here~~In this section, we update the validation to
 303 include the effects of river flow and compare our results against idealized Delft-3D numerical
 304 model results ~~that are run under~~using the same bathymetry and forcing (Type I). Then, we compare
 305 our analytical model results against an idealized numerical model developed for the Cape Fear
 306 Estuary, North Carolina (Familkhalili and Talke, 2016). This numerical model simulates storm
 307 surge from tropical storms by using a parametric model of hurricane wind and pressure forcing
 308 that is applied over the continental shelf (Type II). Table 1 shows the model parameters that were
 309 used to compare analytical model results with numerical models.

310 Table 1. Analytical model parameters used in this study. See Appendix for a description of
 311 parameters. Non-dimensional river discharge (θ) is applied at the upstream boundary and tide and surge
 312 waves are applied at the ocean boundary (i.e., the estuary mouth, $x=0$ in Fig 1).

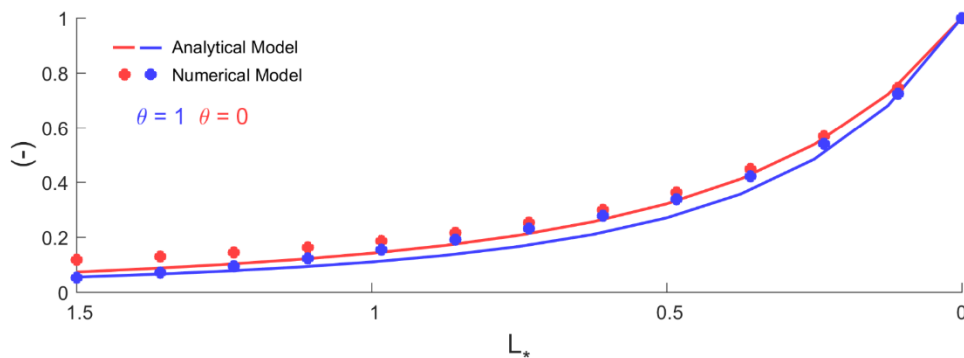
<i>Type</i>	B_0 (km)	L (km)	L_e (km)	B_c (km)	L_c (km)	h (m)	θ	<i>Tide</i> { Amp. (m) } { Period (h) }	<i>Surge</i> { Amp. (m) } { Period (h) }
I	5	120	80	1.1	100	5-7-10-15	0-0.25-0.5-1	{0.5} {12}	{0.5} {24} + {0.25} {8}
II	3	30	20	0.7	100	7-10-13-15	0	{0.5} {12}	{0.5} {12} + {0.25} {6}

313

314 **3-1- Idealized numerical models with similar forcing**

315 -Analytical/numerical comparisons were made for a weakly convergent and strongly dissipative
 316 estuary with constant depth of 5m and a width profile defined by Type I (Table 1, $B_0=5$ km, L_e
 317 $=80$ km (see Fig. 1). The estuary section of the model domain (L) is 120 km, 1.5 times the
 318 convergence length. Both analytical and numerical models are forced by the K_1 , M_2 , and M_3 tidal
 319 constituents at the ocean boundary, two of which (K_1 and M_3) combined represent a surge wave
 320 (Table 1). We further analyze the numerical model results by using harmonic analysis (e.g., Leffler
 321 and Jay, 2009).

322 Figure 3 shows the spatial pattern of the dominant tidal constituent (M_2) amplitude normalized by
 323 its value at the estuary mouth. The analytical model results closely resemble the numerical model
 324 results with a root-mean-square error of 0.02 m for both the three-wave model with and without
 325 river flow (blue and red colors in Fig. 3), showing that this idealized analytical model can properly
 326 estimate spatial variability of surge along an estuary.

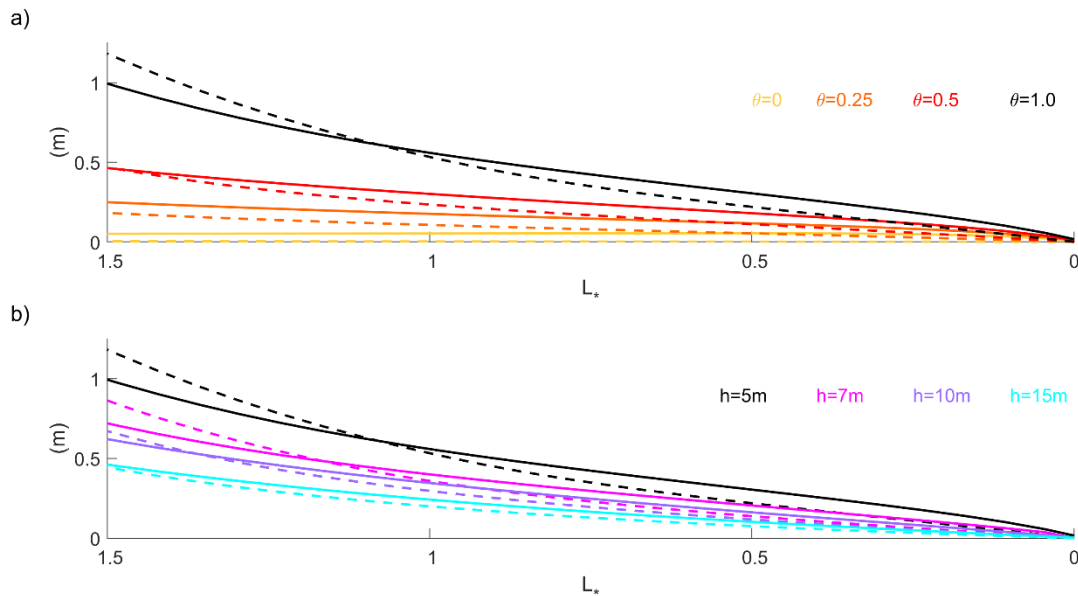


327
 328 Figure 3. Dominant tidal constituent (M_2) amplitude in a 5 m deep estuary for three tides models (K_1 , M_2 , and M_3)
 329 with and without river flow ($\theta=0-1$). The x axis is the estuary length normalized by the convergence length scale
 330 ($L_* = x/L_e$) and the vertical axis is normalized by M_2 amplitude at the ocean boundary ($L_*=0$).

331 In addition, results for the tidally averaged water levels (i.e., Z ; see Fig. 1) under conditions
 332 conditions with both of tidal and river-flow forcing are consistent with numerical models, as shown
 333 in Fig. 4 for a weakly convergent estuary. The water level profiles vary with θ (normalized flow
 334 velocity) for both the analytical model (dashed lines) and the numerical model (solid lines). In
 335 general, the analytical model slightly underestimates numerical results. The root-mean-square
 336 deviation RMSE between the numerical and analytical surface profiles are 0.03, 0.08, 0.09, and
 337 0.10m for a θ of 0, 0.25, 0.5, and 1.0, respectively, or roughly 3-8 % of the total super-elevation
 338 above sea-level (Fig. 4a). The pattern seen in Fig. 4 can be explained by Eq. (8), in which as river
 339 discharge increases (greater θ), the depth averaged velocity increases, and a larger water surface
 340 slope ($\frac{\partial H}{\partial x}$) is needed to balance the Eq. (8).

341

342



343

344

345

346

347

348

Figure 4. (a) The importance of river flow (i.e., θ at $L_*=1.5$) for 5m depth and (b) the importance of channel depth for $\theta=1$ in an idealized three sinusoidal-waves model. The vertical axis is tidally averaged water level and horizontal axis represents dimensionless coordinate system of $L_* = x/L_e$. Solid and dashed lines represent numerical and analytical model results, respectively. The black solid and dashed lines represent same scenario ($h=5$ m, $\theta=1$) in both (a) and (b).

349

3-2- Idealized numerical model with parametric hurricane forcing

350

351

352

353

354

355

356

357

358

359

360

361

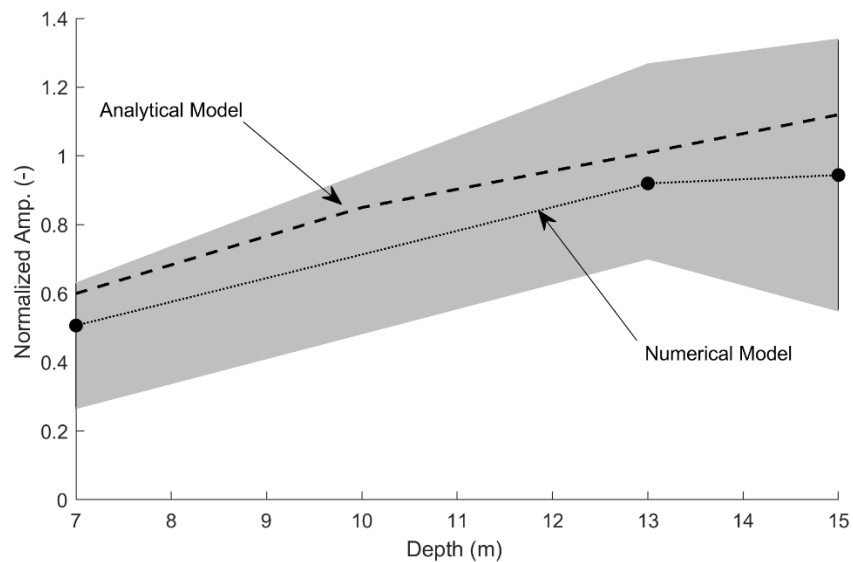
362

363

364

We further validate our analytical model results (Type II) with the idealized numerical modeling of Familkhalili and Talke (2016). This model includes a storm surge produced at the continental shelf and six semidiurnal and diurnal tidal constituents. Upstream of river kilometer 12, the estuary is convergent with an e -folding length scale of ~ 20 km. The analytical model uses similar geometry (Table 1), uses the dominant tidal constituent (M_2) at the estuary mouth and assumes that the primary surge wave has a period of 12 h. As in the numerical model, river flow is set to zero (Table 1). We compare our analytical results at $\sim L_* = 1.5$ with the corresponding location in the numerical model (Wilmington, North Carolina). For a shallow estuary of 7 m, the analytical model suggests that the storm surge wave is damped by $\sim 40\%$ (from 0.5 m to 0.3 m) between the coast and $L_* = 1.5$ (Fig. 5). This damping is within the range of modeled results for a tropical storm surge at Wilmington ($L_* \sim 1.5$, Fig. 5). In a deeper configuration (mean depth = 15 m), the analytical model (this paper) finds a 12% increase in surge amplitude from the coast, well within the normalized amplitude of 0.55-1.35 found in Familkhalili and Talke (2016). Hence, both the sense of change as depth increases and the order of magnitude of change is consistent between the numerical and analytical model, improving our confidence in results (Fig. 5).

365



366

367 Figure 5. Comparison of normalized surge amplitude as a function of depth for an estuary resembling the Cape Fear
 368 Estuary at an inland location at the approximate location of Wilmington, North Carolina. The dashed line is the
 369 analytical model result, and the solid line is the numerical result. The idealized numerical model uses a surge event
 370 with a mean amplitude of 0.6m at the ocean boundary (data from Familkhalili and Talke 2016). The fill area is the
 371 range of results due to different relative phase of the storm surge and tide wave. The ‘Analytical model’ results are
 372 for a 12 h surge that had an amplitude of 0.5 m and is evaluated at $L_* = 1.5$, at the approximately same location as
 373 the numerical model. The y-axis is normalized surge amplitude and equals one at the ocean boundary.

374 The results of the model comparison (Fig. 3, 4 and 5) show that both the analytical and idealized
 375 numerical models produce broadly consistent results. Therefore, our neglect of acceleration in the
 376 subtidal model (Fig. 4) and the use of linearized friction is justified. Both numerical and analytical
 377 models are complementary tools. A 3D model with resolved bathymetry is clearly best used to
 378 evaluate the specific effect of bathymetric alterations in a particular estuary (e.g., Pareja-Roman
 379 et al., 2020; Helaire et al., 2020), or to run simulations using complex, real valued boundary forcing
 380 (river and coastal). But our analytical model runs substantially more quickly than even the
 381 idealized numerical models, facilitating investigation of a larger parameter space. Moreover,
 382 numerical models cannot unambiguously separate tide, fluvial, and surge effects. Currently, the
 383 best-practice approach is to run the numerical model with and without relevant forcing; for
 384 example, by running a surge model with and without tides, one can approximate the effect that
 385 tides have on total water level (Shen et al. 2006). When combined, tide and surge wave travel
 386 faster (due to deeper water depth; see Horsburgh and Wilson, 2007), and frictional energy loss in
 387 each wave component is also larger (Familkhalili et al., 2020). Due to the multiple feedbacks and
 388 nonlinear interactions, decomposing numerical results into individual surge and tide wave
 389 transformations is inherently ambiguous. The analytical approach, while not including all
 390 interactions (such as the phase modulation caused by depth variability), is able to individually
 391 estimate transformations in the primary surge and tide constituent amplitudes, also under
 392 conditions of different river discharge. This approach, to our knowledge, has not previously been

393 approached to understanding the fundamental bathymetric and boundary condition factors that
 394 influence compound events.

395

396 **4- Dimensional and non-dimensional parameter space studied**

397 We use our validated analytical model to further investigate the effects of channel depth, river
 398 flow, channel width convergence, and surge time scale on the spatial evolution of water levels
 399 along estuaries. For all simulations, the primary tidal constituent period and amplitude are fixed to
 400 12 h (i.e., a semidiurnal or D_2 wave) and 0.5 m, respectively, a value that is typical of the semi-
 401 diurnal tide wave on the U.S. East Coast (Table 1). To study the effects of width convergence, we
 402 test both weakly ($L_e=80$ km) and strongly convergent ($L_e=20$ km) conditions (see e.g., Jay, 1991;
 403 Lanzoni and Seminara, 1998). Table 1 shows the parameter space used in the model. The primary
 404 and secondary surge amplitudes are set to be 0.5 and 0.25 m, respectively (Eq. (6)) and the estuary
 405 mouth (B_0) is assumed to have a width of 5 km. ~~A-S~~ sensitivity analysis is ~~done-carried out~~ by
 406 varying the parameters in Table 1 individually, with other parameters held constant, resulting in a
 407 total of 128 parameter combinations (i.e., four different values for depths, four different values for
 408 river flow, four different periods combination, and two convergence length scales).

409

Table 1: Parameter space used in analytical model

<i>Channel Depth (m)</i>	5, 7, 10, 15
<i>Su_{Pri} Amp. (m)</i>	0.5
<i>Su_{Sec} Amp. (m)</i>	0.25
$\begin{pmatrix} Su_{Pri} \text{ Period (hr)} \\ Su_{Sec} \text{ Period (hr)} \end{pmatrix}$	$\begin{pmatrix} 12 \\ 6 \end{pmatrix}, \begin{pmatrix} 24 \\ 12 \end{pmatrix}, \begin{pmatrix} 48 \\ 24 \end{pmatrix}, \begin{pmatrix} 72 \\ 36 \end{pmatrix}$
<i>D₂ Amp. (m)</i>	0.5, 1
<i>D₂ Period (h)</i>	12
<i>D₁ Amp. (m)</i>	0.5, 1
<i>D₁ Period (h)</i>	24
<i>Upriver flow velocity ($\theta = \frac{ u_r }{ u_{D_2} }$) at $L_* = 1.5$</i>	0, 0.25, 0.5, 1
<i>Convergence length scale, L_e (km)</i>	80 (weakly convergent), 20 (strongly convergent)

410

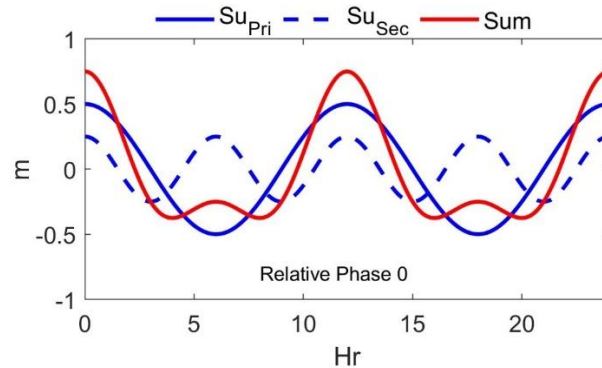
411 Non-dimensional variables provide insights into which parameters produce the most effect on
 412 system response. From the scaling of Eq. (3) (see also Familkhalili et al., 2020), we derive the
 413 three most relevant independent non-dimensional variables:

- 414 • Parameter (Ω) represents the ratio of Su_{Pri} period to D_2 period and represents the
 415 influence of primary surge wave period on tide-surge interactions.
- 416 • The friction number ($\psi = \frac{c_d \xi \omega^2 L_e^3}{gh^3}$) shows the effects of changing surge wave
 417 properties, which are influenced by depth (h), surge frequency ($\omega = \frac{1}{T}$), and
 418 convergence length-scale (L_e); all affect the damping or amplification of surge
 419 waves.
- 420 • Parameter (θ) represents the ratio of upriver velocity (at $L_*=1.5$) to the major tidal
 421 component (D_2) velocity at the estuary mouth.

422 For plotting purposes, we define two additional non-dimensional numbers: Su_{Pri} normalized
 423 amplitude ($A_* = \frac{Amp. Su_{Pri}}{Surge Amp. at Ocean Boundary}$) and a dimensionless coordinate system of $L_* =$
 424 x/L_e , where L_* is normalized length.

425 In our models, we assume that the two surge waves are symmetric with a phase lag (ϕ in Eq. (5))
 426 of zero degrees between Su_{Pri} and Su_{Sec} , resulting in a repeating and symmetric storm surge wave
 427 (see Fig. 65). This simulates a storm surge in which there is initially a draw-down in water level,
 428 followed by the positive storm surge. To test the most frictional case, we also define the relative
 429 phase lag between the D_2 wave and surge to be zero.

430



431 Figure 6. A symmetric surge wave which is the result of two sinusoidal waves (i.e., $Surge = Su_{Pri} + Su_{Sec}$).

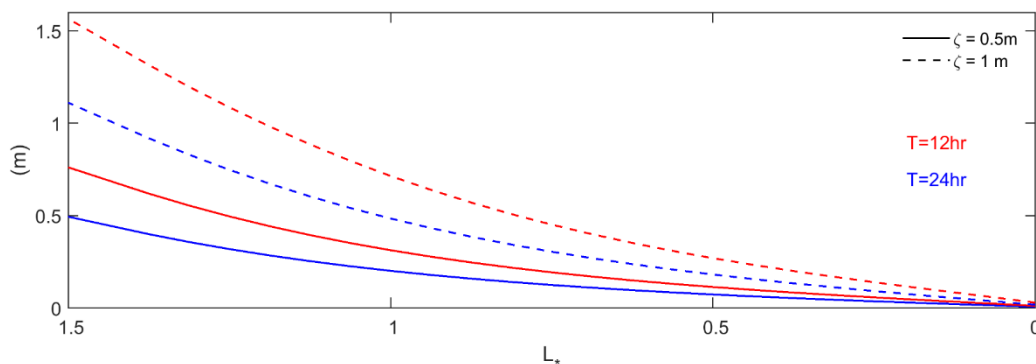
432 5- Results and discussion

433 We employ the validated model to study how bathymetry, river discharge, and surge characteristics
434 affect water floods in an idealized estuary. First, the effects of surge amplitude and period on water
435 levels are examined. Then, the effects of river discharge and width convergence on surge amplitude
436 are presented, and finally compound flooding of tide, surge, and river flow is investigated.

437 5-1- Effects of wave characteristics on water level

438 The influence of wave characteristics (i.e., period and magnitude) on tidally averaged water level
439 is tested by modeling a set of waves with periods of 12 h and 24 h and amplitudes of 0.5 m and 1
440 m at the ocean boundary (i.e., D_1 and D_2 in Table 1). Model results confirm, as suggested by the
441 friction number (ψ), that increasing wave period ($T = \frac{1}{\omega}$) or decreasing wave amplitude (ζ) has
442 similar effect as increasing depth (h) and therefore would result in lower mean water levels (see
443 Fig. 67). Figure 6-Specifically, increasing wave period from 12_h (red lines) to 24_h (blue lines)
444 would-reduces the mean water level at $L_* = 1.5$ from 0.75 m to 0.5 m, and from 1.56 m to 1.10 m
445 for wave amplitudes of 0.5 m and 1 m at the ocean boundary ($L_* = 0$), respectively. In other words,
446 for the same boundary amplitude, a shorter period wave produces larger mean water levels
447 landward.

448



449

450 Figure 7. The effects of wave period (i.e., 12 h and 24 h) and amplitude (0.5 m and 1m at the ocean-boundary $L_* = 0$)
451 on tidally averaged water level for 5 m depth channel in an idealized one sinusoidal wave model for $\theta=1$. Vertical

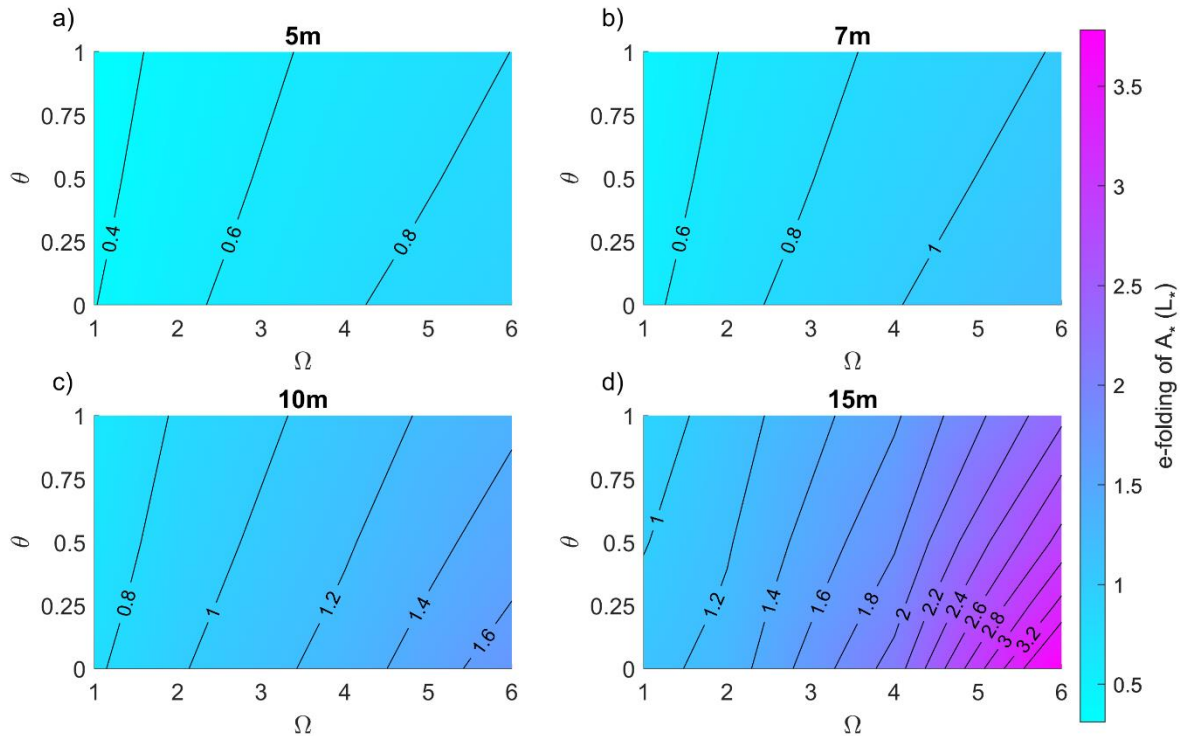
452 axis is tidally averaged water level, and the horizontal axis represents the estuary length normalized by the
453 convergence length scale (i.e., $L_* = x/L_e$).

454 **5-2- Frictional effects of river discharge on surge amplitude**

455 The rate at which a surge decays away from the ocean entrance varies with river flow and surge
456 period. Figure 8 shows the effects of river discharge and surge period on the e -folding length-scale
457 of Su_{pri} normalized amplitude (A_*); ~~the e -folding length is defined as the distance~~ required for
458 ~~A_* to get reach to~~ $1/e \sim 38\%$ of boundary values). The longer the wave period, the more slowly
459 surge normalized amplitude A_* decreases as the surge moves landward (keeping all other variables
460 constant). For example, Fig. 8a shows that a 12 h ($\Omega = 1$) surge amplitude reaches an e -folding
461 reduction in amplitude at $\sim 0.4L_*$ compared to $\sim 0.9L_*$ for the 72 h ($\Omega = 6$) surge. The lower rate of
462 spatial decay of surge amplitude for lower frequency surge waves is caused by their lower velocity
463 and consequent smaller frictional effects.

464 Model results also show that higher river discharge will increase the damping of surge amplitudes
465 (Fig. 8). When ($\theta = 0$), river flow is zero and only tide-surge nonlinear interactions can occur.
466 Hence, surge amplitudes decay more slowly for $\theta = 0$ than for $\theta > 0$ (compare the $\theta = 0$ and $\theta =$
467 1 cases in Fig. 8). The slanted contour lines highlight the effects of river flow; as θ increases, the
468 e -folding length-scale of normalized amplitude (A_*) reduces for all surge periods ($\Omega = 1-6$) (Fig.
469 8a-d). Adding river flow to a surge with a primary period of 12 h ($\Omega = 1$) reduces the e -folding
470 scale of damping from $0.4L_*$ ($\theta = 0$) to $0.34L_*$ ($\theta = 1$), for the 5 m depth case ($\sim 15\%$ decrease;
471 Fig. 8a). The percent decrease in the e -folding scale is larger in a deeper, 15m channel, and
472 decreases from $1.15L_*$ to $0.95L_*$ ($\sim 18\%$ decrease; Fig. 8d).

473 Surge amplitudes also decay more slowly (larger e -folding) in a deeper channel for all surge
474 periods (Fig. 8). ~~Thus that~~, the largest difference in normalized amplitude between a 12 h ($\Omega = 1$)
475 and 72 h ($\Omega = 6$) surge occurs at larger depth ($h = 15$ m) with changes of $\sim 1L_*$ to $3.5L_*$ in the e -
476 folding length-scale of damping (Fig. 8d). Increasing the river discharge relative to the M_2 velocity
477 (larger θ) reduces the amplification of the surge wave and therefore the e -folding length scale of
478 A_* reduces from $\sim 3.5L_*$ to $\sim 2.4L_*$ for Su_{pri} of 72 h (Fig. 8d).



479

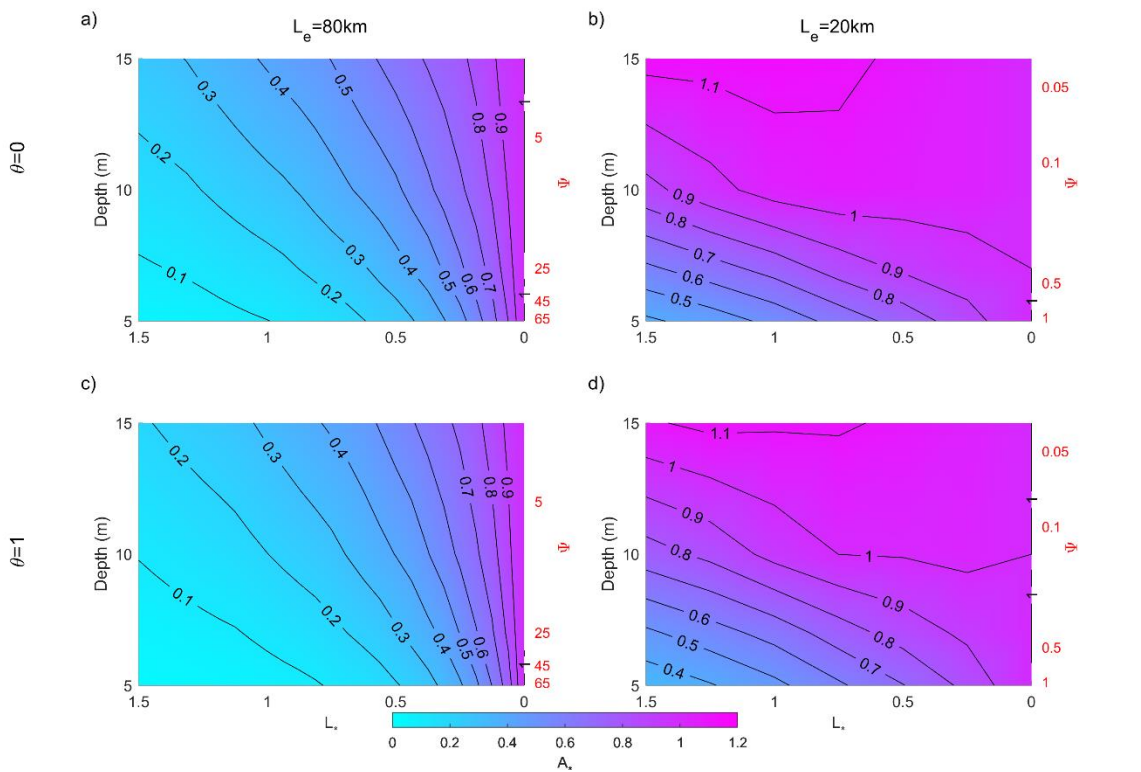
480 Figure 8. The effects of river flow ($\theta = \frac{|u_r|}{|u_{D2}|}$) and surge periods ($\Omega = \frac{Supri\ Period}{D_2\ Period}$) along an idealized weakly
 481 convergent estuary for channel depth of (a) 5 m, (b) 7 m, (c) 10 m, and (d) 15 m. The color scaling represents the e -
 482 folding length-scale of primary surge normalized amplitude (A_*).

483 Consistent with other studies (e.g., Kukulka and Jay, 2003b; Hoitink and Jay, 2016), both the
 484 analytically and numerically modeled water level slope ($\frac{dz}{dL_*}$) is largest upstream and becomes
 485 significantly less near the coast. This is drivencaused by the decreased river velocity (and friction)
 486 associated with the downstream due to the increase in cross-sectional area in the estuary.
 487 Therefore, we expect that varying the forcing or the geometry will conditions will most impact
 488 mean water levels more-upstream, dues to greater total river velocity magnitudes shift in the
 489 landward part of the system.

490 5-3- Effects of width convergence on surge amplitude

491 Long-wave propagation along an estuary is characterized by a balance of inertial effects, friction,
 492 and convergence. Figure 9 shows the normalized amplitude (A_*) of the primary surge wave for
 493 weakly convergent (left panel, 98a and 98c) and strongly convergent estuaries (right panel, 98b
 494 and 98d), for a 12 h surge period ($\Omega = 1$). The contours represent the e -folding length-scale of
 495 primary surge normalized amplitude and the x -axis represents the dimensionless coordinate system
 496 of $L_* = x/L_e$. The factor 4X change in convergence length scale from 80 km (Fig. 98a, 98c) to 80
 497 km (Fig. 98b, 98d) alters the friction scale (ψ) by a factor of 64.

498 The convergence of an estuary influences surge amplitudes (Fig. 98), similar to its well-known
 499 effects on tidal amplitudes (e.g., Jay, 1991). All surge amplitudes decrease landward for all depth
 500 cases in a weakly convergent ($L_e=80$ km) estuary; effectively, convergence effects are much
 501 smaller than the bed friction and gravity effects and therefore long-wave amplitudes decrease (Fig.
 502 98a and 98c). Under strongly convergent conditions with no river flow, the primary surge
 503 amplitude decays less quickly in a deeper channel as it moves upstream than under weakly
 504 convergent condition (see Fig. 98a, b), and can even increase in the inland direction (see Fig. 98b).
 505 By contrast, increased river discharge produces greater damping in the surge wave (compare Fig.
 506 98a and 98c, or Fig. 98b and 98d). For example, for friction factor of $\psi = 0.5$ ($h = 6.5$ m) and a
 507 location of $L_* = 1$, the surge wave has damped to 60 % of its boundary value when the tidal to
 508 river flow ratio is $\theta=1$ (Fig. 98d) but is at 70 % of its boundary value when there is no river
 509 discharge (Fig. 98b). Hence, increasing river flow and decreasing channel depth both cause larger
 510 damping in the surge wave.



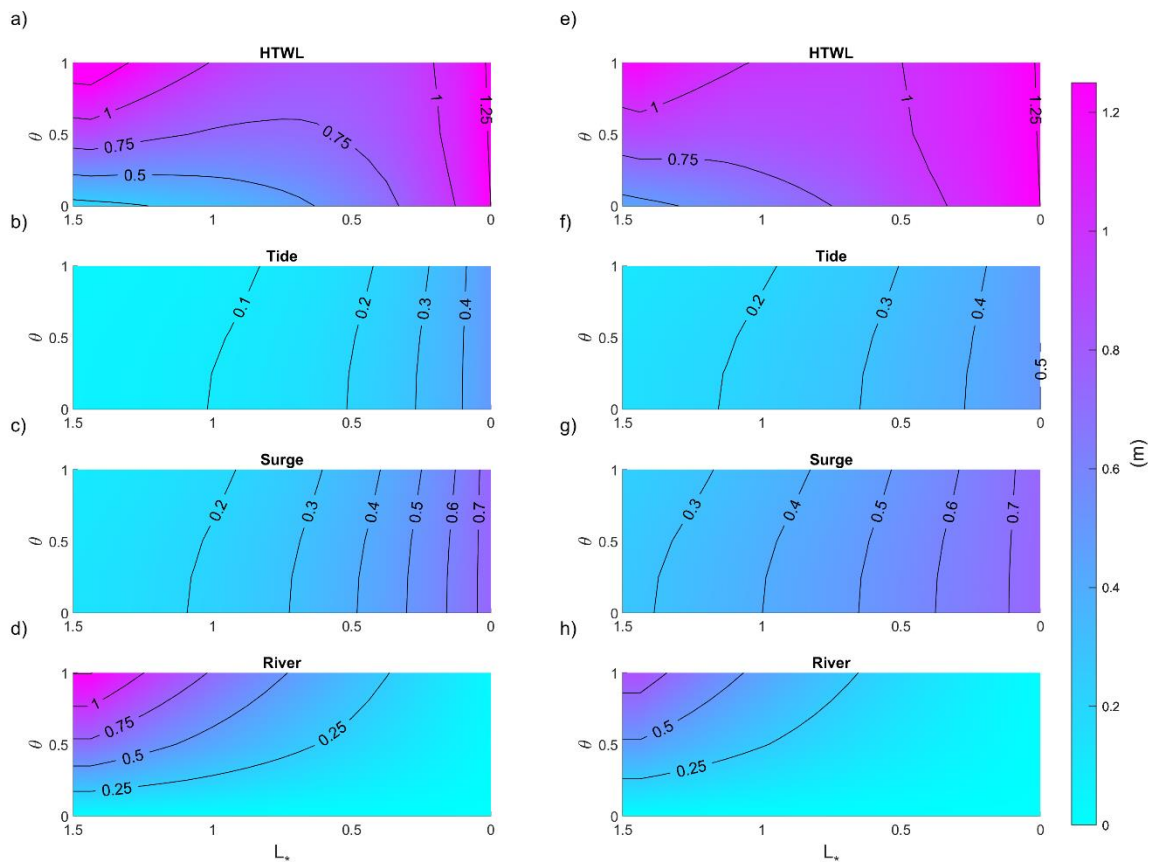
511
 512 Figure 9. The effects of convergence length scale and river discharge on primary surge ($12_h, \Omega = 1$) amplitude (A_* is
 513 normalized amplitude) along a weakly convergent estuary, $L_e=80$ km (subplots a, c) and strongly convergent
 514 estuary, $L_e=20$ km (subplots b, d). Left hand side vertical axis is channel depth and right-hand side vertical axis is

515 the corresponding non-dimensional friction number ($\psi = \frac{C_d \xi \omega^2 L_e^3}{gh^3}$) and horizontal axis represents dimensionless
 516 coordinate system of $L_* = x/L_e$.

517 **5-4- Combined effects of tide, surge, and river flow on total water levels**

518 We next investigate how variations in river flow influence the Total Water Level (TWL), **which**
 519 **caused by** the combination of tide, storm surge, and river discharge effects ($TWL = T + SS + R$).
 520 The highest possible total water level (HTWL) during such a compound event occurs when the
 521 ~~tide (D_x) and surge have zero relative phase (i.e., the surge occurs at high water,) and when~~
 522 coincident with the peak river flow. Because the timing of a meteorological event is usually
 523 random relative to tides, and because peak surge usually precedes peak river discharge, HTWL
 524 rarely if ever occurs. However, it is a useful metric of the potential flooding. Such a worst-case
 525 scenario could occur, for example, when multiple storms occur in close succession. The HTWL
 526 therefore provides a way to compare different parameter regimes and evaluate the effect of long-
 527 term changes in the geometry of an individual estuary.

528



529
 530 Figure 10. Combined contribution of tide, surge, and river flow to water level for depths of 5 m (left panel subplots)
 531 and 10 m (right panel subplots). Colors and the labeled contours denote water level. The total water level (a and e) is

532 the combination of tidal amplitude (b and f), surge amplitude (c and g) and water level from river discharge (d and
533 h). The period of the primary surge (Su_{pri}) is 24 h, the convergence length scale is 80km, the x -axis represents
534 dimensionless coordinate system of $L_* = x/L_e$ (origin at estuary mouth, on right-hand side) and the y -axis shows the
535 non-dimensional river flow ($\theta = \frac{|u_r|}{|u_{D_2}|}$).

536 The HTWL (Fig. 109a and 109e) follows a pattern set by the contradictory effects of river flow
537 and marine forcing (tides and surge). Far upstream ($L_* = 1.5$), river water levels are the largest
538 factor, particularly for larger θ , ~~and-but~~ decay in the downstream direction (Fig. 9d-10d and
539 9h-10h). The surge and tidal components of water level (e.g., Fig. 9b-10b, 9e-10e) decay in the
540 opposite direction, from the oceanic boundary towards the upstream boundary. For larger river
541 flows ($\sim\theta>0.5$), the counteracting factors produce a minimum HTWL in the middle part of the
542 domain ($L_* = 0.5-1.0$). For small river flows, water levels monotonically decrease in the upstream
543 direction.

544 Importantly, the HTWL is not merely the superposition of river flow, tide, and surge effects,
545 considered in isolation. Rather, as shown by the non-vertical contour lines for tides and surge (e.g.,
546 Fig. 9f-10f and 9g-10g), increases in the relative influence of river flow (larger θ) tend to reduce
547 the magnitude of tides and surge (see also Helaire et al., 2020). By contrast, increases in long-
548 wave magnitudes (tides, surge) at the ocean boundary increase the tidally averaged water level
549 profile, as already established (Fig. 67; see also Buschman et al., 2009 and Talke et al., 2021).
550 Simultaneously, long-wave magnitudes decrease more quickly, the larger they are at the estuary
551 ocean boundary (see also Familkhalili et al., 2020). Effectively, each component of water level
552 influences the other, and itself: for example, tides within the domain depend on self-interaction
553 (e.g., the boundary magnitude matters), and also on tide-surge and tide-river interaction. While the
554 overall influence in terms of magnitude is relatively minor for the parameter space in Fig. 10, these
555 observations show that non-linear tide-surge-river interactions during a compound event cannot
556 be neglected. -In particular, interactions would be larger in macrotidal systems, and/or for larger
557 surges.

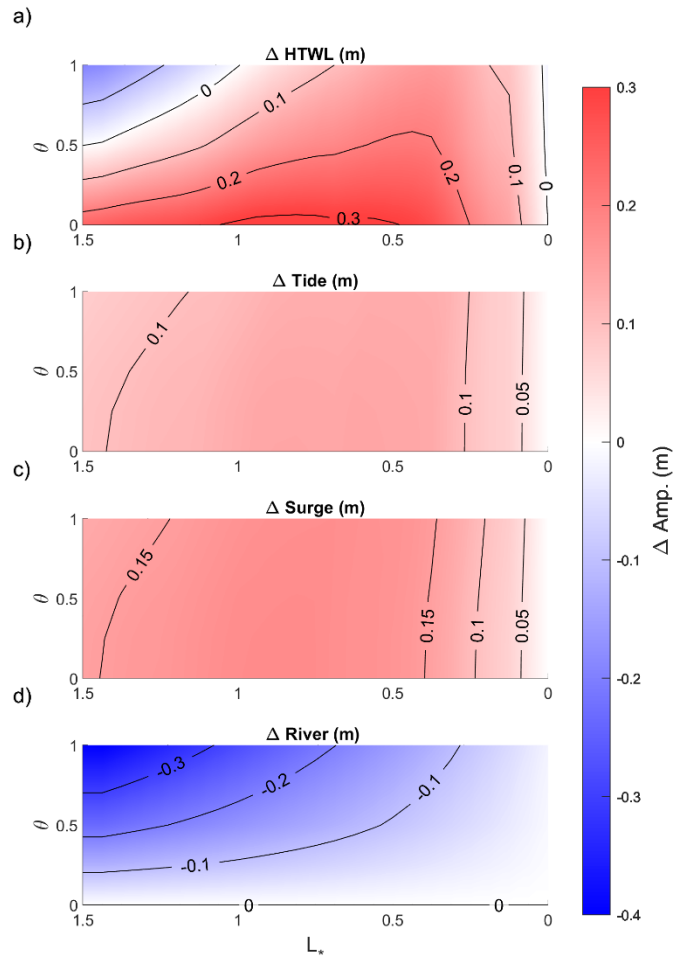
558 Changes in the depth of an estuary, whether by dredging, sea-level rise, or
559 sedimentation/erosion morphodynamic change, also exert a strong, spatially variable influence on
560 the HTWL (Fig. 109 and 114). When depth is small (5m; Fig. 9a-10a), the HTWL is greater in the
561 upstream domain ($L_* = 1.5$ and $\theta>0.5$) than in a larger depth case (10m; Fig. 9e-10e). This occurs
562 because a larger average river slope is needed to push the same amount of water seaward when
563 depth is small, as suggested by Eq. (8) (see also Talke et al., 2021). However, smaller depths also
564 lead to greater dissipation and frictional effects in the tide and surge wave, due to the same
565 reduction in hydraulic drag (compare right-hand and left-hand side of Fig. 9-10, and their difference
566 (Fig. 10-11)). Hence, tide and surge amplitudes increase when depth is increased, for all river
567 discharges ($\theta = 0-1$; Fig. 10b-11b, c). The percent increase is less for higher river discharge; this is
568 evident from the shown by the contours that slant rightward slant of contours in- (Fig. 10b-11b and
569 10e-11c). Further, both tides and surge show a region of maximum change, located in mid-estuary

570 (between $L_* = 0.5$ to 1; Fig. 4011). Near the ocean boundary, changes are relatively small, also in
571 percentage terms. Far upstream, the percent change in tidal range may still be significant, but the
572 magnitudes themselves are small (see also Talke et al., 2021).

573 The differences in the response of river flow and storm surge to a depth increase lead to a *crossover*
574 *point*, which we define as the location in which river flow effects on HTWL are larger than marine
575 effects, for a given set of forcing conditions (see the zero-contour line in Fig. 40a11a). Since the
576 crossover point moves upstream as depth increases (Fig. 4412), processes such as dredging,
577 erosion, or sea-level rise that increase depth can alter the relative influence of marine and river
578 effects, for a given storm surge and river flow. Similarly, a decrease in mean river dischargeinflow,
579 as has occurred in many river-estuaries due to flow regulation, may also cause a landward
580 migration in the crossover point (Fig. 4412).

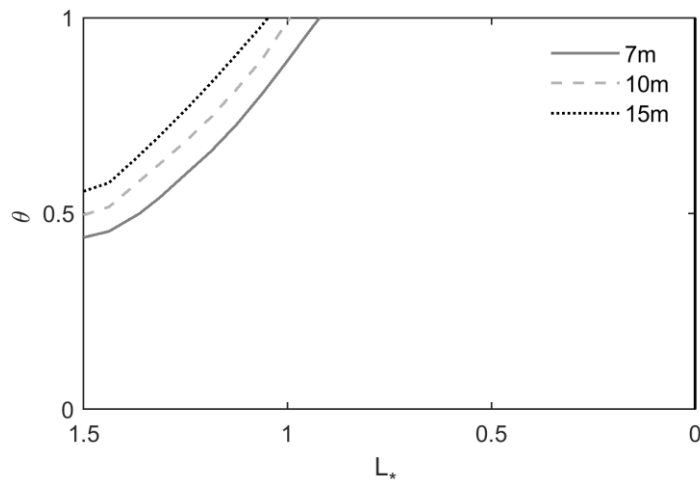
581 Other factors that influence long-wave amplitudes also influence the crossover point, including the
582 period of the surge (Fig. 78), convergence length L_e (Fig. 89), the boundary amplitude, and the
583 relative phasing of tides and surge (see Familkhalili et al., 2020). The influence of many of these
584 factors is explained by considering the non-dimensional friction number ($\psi = \frac{C_d \xi \omega^2 L_e^3}{gh^3}$) (see Sect.
585 2.1). This number suggests that increases in channel depth (h) and, wave period ($T = \frac{1}{\omega}$), and
586 decreases in length scale (L_e) have similar effects on wave amplitudes. For example, increasing
587 the depth from 5 m ($\psi = 69$) to 15 m ($\psi = 2.6$) causes A_* (i.e., normalized amplitude by ocean
588 boundary amplitude) to increase from ~ 0.06 to 0.26 (Fig. 8a9a). Similarly, changing the surge
589 period from 12 to 60 h ($\psi = 69$ to 2.8) changes A_* from ~ 0.06 to 0.22 for a 5 m channel depth.

590 Other studies,s such as Bilskie and Hagen (2018), have defined flood zone transitions between
591 marine and fluvial dominance; close to coast, tide and surge-based flooding dominates, while river
592 floods dominate far upstream. In between, there is a transition zone with compound flooding in
593 which both coastal and fluvial processes are important. Here, our model also suggests that the
594 transition zone location is sensitive to changes in estuary geometry, such as depth, in addition to
595 being dependent on the relative strength of river flow, tide, and surge amplitudes.



596

597 Figure 11. Comparison of contribution of tide, surge, and river flow to compound flooding between 5 m and 10 m
 598 depth channel and $Su_{pri} = 24$ h. Δ represents the amplitude difference of each subject factor (HTWL, tide, surge, and
 599 river flow) between two controlling depths. The convergence length scale is 80 km and x-axis represents dimensionless
 600 coordinate system of $L_* = x/L_e$ and y-axis shows non-dimensional river flow ($\theta = \frac{|u_r|}{|u_{D2}|}$).



601

602 Figure 12. Crossover point location for 7-15_m channel depth compared to 5m case, ($Su_{Pri} = 24$ h and $L_e = 80$ km). x -
603 axis represents dimensionless coordinate system of $L_* = x/L_e$ and y -axis shows non-dimensional river flow ($\theta =$
604 $\frac{|u_r|}{|u_{D2}|}$).

605 6- Conclusion

606 In this study, we have applied a new river-tide-surge analytical model to investigate the
607 interactions of tide, surge, and river flow along idealized estuaries. The novelty of our approach is
608 that we develop a quasi-linear analytical model, previously applied to tides, that considers the non-
609 linear interaction between tides, storm surge, and river discharge. To the best of our knowledge,
610 these processes (river flow + surge + tides) have not been explored within an analytical framework.
611 The model also elucidates the trade-offs caused by channel deepening, which can reduce mean
612 water levels but increase storm surge and tides.

613 -We show that the rate of damping in a storm tide (surge + tide) is sensitive to fluctuations of river
614 discharge (Fig. 78), alterations in the surge period (Fig. 78), and channel geometry changes (~~depth~~
615 ~~and~~ width convergence and depth) (Fig. 89). Model results show that the crossover point, which
616 is the location at which the river flow effects are larger than marine effects, moves upstream as
617 channel depth increases or as river flow decreases (Fig. 12). Thus, the spatial variability in
618 compound flood risk contributors (i.e., tide, surge, and river flow) change when an estuary is
619 modified, or river discharge changes. Generally, increasing the surge period has a similar effect as
620 increasing the depth; however, we note that our model is slightly more sensitive to depth, due to
621 the cubic relationship in the friction term, rather than the squared effect of period. The non-
622 dimensional friction number (ψ) suggest that the effects of surge amplitude at boundary (ξ) and
623 drag coefficient (C_d) have a lesser, but still important, influence on the spatial damping of surge
624 as the depth. We conclude that in a shallow estuary the effects of friction are dominant over the
625 convergence and cause the wave amplitudes (tides and surge) to decrease, while deepening the
626 estuary may cause amplification of long-waves upriver of an estuary. As shown in Fig. 9, the
627 amplification in storm surge is particularly acute when the estuary is highly convergent.

628 Globally, natural and local anthropogenic changes in estuaries (e.g., sea-level rise, channel
629 deepening for navigation and landfilling) produce alterations in tidal and surge amplitudes (see
630 review by Talke and Jay, 2020, and references therein). This study shows that river flow and its
631 interaction with tides and surge must also be considered when evaluating changes to water levels.
632 For example, increasing the river discharge relative to tide velocity reduces the amplification of
633 the surge wave. Moreover, channel deepening produces a reduction in the water level caused by
634 river discharge, leading to a domain in which channel deepening produces lower water levels
635 upstream but larger water levels in the estuary (Fig. 9-12; see also Helaire et al, 2019 and
636 Ralston et al., 2019). Our findings are consistent with other studies that find that reduced frictional
637 effects (e.g., caused by channel deepening) can cause increases to tides and surge (see e.g., Ralston

638 et al., 2019; Talke et al., 2021). Overall, anthropogenic changes to estuary geometry and frictional
 639 characteristics can cause large changes in the amplitude and spatial distribution of compound
 640 flooding. Hence, the spatial characteristics of compound flooding may shift over time due to
 641 anthropogenically-induced changes to geometry.

642 7- Appendix

643 This glossary provides definitions of the terms used in this manuscript.

Name	Definition	Unit
A	<u>Channel cross-sectional area</u>	m^2
A_*	<u>Ratio of primary surge amplitude within the estuary to the surge wave amplitude at ocean boundary</u>	=
b	<u>Channel width</u>	m
B_0	<u>Estuary mouth width</u>	m
B_c	<u>River width</u>	m
C_d	<u>Drag coefficient</u>	=
D_1	<u>Diurnal tidal constituent</u>	=
D_2	<u>Semidiurnal tidal constituent</u>	=
g	<u>Gravitational acceleration</u>	ms^{-2}
h	<u>Channel depth</u>	m
K	<u>Bed stress divided by water density</u>	m^2s^2
L	<u>Length of estuary</u>	m
L_e	<u>Convergence length scale of estuary width</u>	m
L_c	<u>Constant width river channel length</u>	m
L_*	<u>Normalized length</u>	=
Q	<u>Cross-sectionally integrated flow</u>	m^3s^{-1}
Q_R	<u>River flow discharge</u>	m^3s^{-1}
Q_T	<u>Tidal transport</u>	m^3s^{-1}
Su_{pri}	<u>Primary surge wave</u>	=
Su_{sec}	<u>Secondary surge wave</u>	=
t	<u>Time</u>	s
T	<u>Surge period</u>	s
u_R	<u>River flow velocity</u>	ms^{-1}
u_T	<u>Tidal velocity</u>	ms^{-1}
U_R	<u>Maximum river flow velocity</u>	ms^{-1}
U_T	<u>Maximum tidal velocity</u>	ms^{-1}
x	<u>Along channel distance. Estuary mouth is at $x = 0$ and x increases landward</u>	m
ξ	<u>Tidal amplitude</u>	m
θ	<u>River velocity magnitude to the magnitude of the major tidal component velocity at the ocean boundary</u>	=

ρ	<u>Water density</u>	<u>$Kg\ m^3$</u>
ϕ	<u>Wave phase</u>	<u>rad</u>
ω	<u>Wave frequency</u>	<u>s^{-1}</u>
Ω	<u>Ratio of primary surge period to main tidal component period</u>	<u>-</u>
ψ	<u>Friction number</u>	<u>-</u>

644

645 **8- Author contribution**

646 Ramin Familkhalili: Methodology, Software, Validation, Formal analysis, Investigation, Data
647 Curation, Writing - Original Draft, Writing - Review & Editing, Visualization

648 Stefan Talke: Conceptualization, Methodology, Formal Analysis, Resources, Writing - Review &
649 Editing, Supervision, Project administration, Funding acquisition.

650 David Jay: Conceptualization, Methodology, Formal Analysis, Resources, Writing - Review &
651 Editing, Supervision.

652 **9- Competing interests**

653 The authors declare that they have no conflict of interest.

654 **10- Data availability**

655 The data used are listed within the body of the manuscript and references.

656 **11- Acknowledgements**

657 Funding was provided by the US Army Corps of Engineers (award W1927N-14-2-0015) and the
658 National Science Foundation (awards 1455350 and 1854946).

659 **12- References**

660 Bertin, X., N. Bruneau, J.-F. Breilh, A. B. Fortunato, and M. Karpytchev (2012), Importance of
661 wave age and resonance in storm surges: The case Xynthia, Bay of Biscay, Ocean
662 Modell.,42,16–30, doi:10.1016/j. ocemod.2011.11.001

663 Bilskie, M. V. and Hagen, S. C.: Defining Flood Zone Transitions in Low-Gradient Coastal
664 Regions, Geophys. Res. Lett., 45, 2761–2770, <https://doi.org/10.1002/2018GL077524>,
665 2018.

666 [Brandon, C.M.; Woodruff, J.D.; Donnelly, J.P., and Sullivan, R.M., 2014. How unique was](#)
667 [Hurricane Sandy? Sedimentary reconstructions of extreme flooding from New York Harbor.](#)
668 [Scientific Reports, <http://dx.doi.org/10.1038/srep07366>](#)

669 Buschman, F. A., Hoitink, A. J. F., Van Der Vegt, M., & Hoekstra, P. (2009). Subtidal water level
670 variation controlled by river flow and tides. *Water Resources Research*, 45, W10420.
671 <https://doi.org/10.1029/2009WR008167>

672 Cai, H., H. H. G. Savenije, and M. Toffolon (2014), Linking the river to the estuary: influence of
673 river discharge on tidal damping, *Hydrol. Earth Syst. Sci.*, 18(1), 287–304, doi:10.5194/hess-
674 18-287-2014.

675 Dronkers, J. J. (1964), *Tidal Computations in Rivers and Coastal Waters*, North-Holland, New
676 York, 296–304.

677 [Ensing H, de Swart HE, Henk HM, Schuttelaars M. 2015. Sensitivity of tidal motion in well-](#)
678 [mixed estuaries to cross-sectional shape, deepening, and sea level rise: an analytical study.](#)
679 [Ocean Dyn. 65:933–50](#)

680 Familkhalili, R., and Talke, S. A. (2016), The effect of channel deepening on tides and storm
681 surge: A case study of Wilmington, NC, *Geophys. Res. Lett.*, 43, 9138–9147,
682 doi:10.1002/2016GL069494.

683 Familkhalili, R., Talke, S. A., & Jay, D. A. (2020). Tide-storm surge interactions in highly altered
684 estuaries: How channel deepening increases surge vulnerability. *Journal of Geophysical*
685 *Research: Oceans*, 125, e2019JC015286. <https://doi.org/10.1029/2019JC015286>

686 Friedrichs, C. T., and Aubrey, D. G. (1994), Tidal propagation in strongly convergent channels.
687 *Journal of Geophysical Research*, 99(C2), 3321–3336. <http://doi.org/10.1029/93JC03219>

688 Giese, B. S., and D. A. Jay (1989), Modeling tidal energetics of the Columbia River estuary,
689 *Estuarine Coastal Shelf Sci.*, 29(6), 549–571, doi:10.1016/02727714(89)90010-3

690 Godin, G. (1985), Modification of rivertides by the discharge, *J. Waterway, Port, Coastal, Ocean*
691 *Eng.*, 1985, 111(2): 257-274

692 Godin, G. (1991), Compact approximations to the bottom friction term for the study of tides
693 propagating in channels. *Continental Shelf Research* 11 (7), 579–589

694 Godin, G. (1999), The propagation of tides up rivers with special considerations on the upper Saint
695 Lawrence River, *Estuarine, Coastal and Shelf Science*, 48, 307 – 324.

696 Godin, G., Martinez, A., (1994): Numerical experiments to investigate the effects of quadratic
697 friction on the propagation of tides in a channel, *Continental Shelf Research*, Vol. 14, No.
698 7/8, pp. 723-748, 1994

699 Helaire, L. T., Talke, S. A., Jay, D. A., & Mahedy, D. (2019). Historical changes in Lower
700 Columbia River and estuary floods: A numerical study. *Journal of Geophysical Research:*
701 *Oceans*, 124, 7926–7946. <https://doi.org/10.1029/2019JC015055>.

702 [Horsburgh, K. J., and C. Wilson \(2007\), Tide-surge interaction and its role in the distribution of](#)
703 [surge residuals in the North Sea, J. Geophys. Res., 112, C08003,](#)
704 [doi:10.1029/2006JC004033.](#)

705 Helaire, L. T., Talke, S. A., Jay, D. A., & Chang, H. (2020). Present and Future Flood Hazard in
706 the Lower Columbia River Estuary: Changing Flood Hazards in the Portland-Vancouver
707 Metropolitan Area. *Journal of Geophysical Research: Oceans*,
708 <https://doi.org/10.1029/2019JC015928>

709 Horrevoets, A., H. Savenije, J. Schuurman, and S. Graas (2004), The influence of river discharge
710 on tidal damping in alluvial estuaries, *J. Hydrol.*, 294(4), 213–228.

711 Hoitink, A. J. F., and D. A. Jay (2016), Tidal river dynamics: Implications for deltas, *Rev.*
712 *Geophys.*, 54, 240–272, doi:10.1002/2015RG000507.

713 Jay, D. A. (1991). Green’s law revisited: Tidal long-wave propagation in channels with strong
714 topography. *Journal of Geophysical Research*, 96(C11), 20585.
715 <http://doi.org/10.1029/91JC01633>

716 Jay, D. A. and E. P. Flinchem (1997), Interaction of fluctuating river flow with a barotropic tide:
717 A test of wavelet tidal analysis methods, *J. Geophys. Res.* 102:5705 – 5720.

718 Jay, D. A., K. Leffler and S. Degens (2011), Long-term evolution of Columbia River tides, *ASCE*
719 *Journal of Waterway, Port, Coastal, and Ocean Engineering*, 137: 182-191; doi:
720 10.1061/(ASCE)WW.1943- 5460.0000082.

721 Jay, DA, A. Devlin, D. Idier, E. Prococki, and RE Flick, (2021), Tides and Geomorphology: Time
722 Scales and Non-Stationary Processes, *Coastal and Submarine Geomorphology, Treatise on*
723 *Geomorphology*, <https://doi.org/10.1016/B978-0-12-818234-5.00166-8>

724 Johnson, F., White, C.J., van Dijk, A. et al. Natural hazards in Australia: floods. *Climatic Change*
725 139, 21–35 (2016). <https://doi.org/10.1007/s10584-016-1689-y>.

726 Jongman B, Ward PJ, Aerts JCJH. Global exposure to river and coastal flooding: Long term trends
727 and changes. *Global Environmental Change* 2012; 22(4): 823-35

728 Kästner, K., Hoitink, A. J. F., Torfs, P. J. J. F., Deleersnijder, E., & Ningsih, N. S. (2019).
729 Propagation of tides along a river with a sloping bed. *Journal of Fluid Mechanics*, 872, 39–
730 73. <https://doi.org/10.1017/jfm.2019.331>

731 Kukulka, T. & D.A. Jay, (2003a). Impacts of Columbia River discharge on salmonid habitat: 1. A
732 nonstationary fluvial tidal model. *Journal of Geophysical Research* v108 No. C9,
733 doi:10.1029/2002JC001382

734 Kukulka, T. & D.A. Jay, (2003b). Impacts of Columbia River discharge on salmonid habitat: 2.
735 Changes in shallow-water habitat. *Journal of Geophysical Research* v108 No. C9,
736 doi:10.1029/2002JC001829

737 Lanzoni, S., and G. Seminara, On tide propagation in convergent estuaries, *J. Geophys. Res.*, 103,
738 30,793–30,812, 1998

739 Munchow, A. K., Masse, A. K. & Garvine, R. W. 1992 Astronomical and nonlinear tidal currents
740 in a coupled estuary shelf system. *Continental Shelf Research* 12, 471-498.

741 Nicholls, R.J., P.P. Wong, V.R. Burkett, J.O. Codignotto, J.E. Hay, R.F. McLean, S. Ragoonaden
742 and C.D. Woodroffe, 2007: Coastal systems and low-lying areas. *Climate Change 2007:*
743 *Impacts, Adaptation and Vulnerability. Contribution of Working Group II to the Fourth*
744 *Assessment Report of the Intergovernmental Panel on Climate Change*, M.L. Parry, O.F.
745 Canziani, J.P. Palutikof, P.J. van der Linden and C.E. Hanson, Eds., Cambridge University
746 Press, Cambridge, UK, 315-356.

747 Nicholls RJ, Hoozemans FMJ, Marchand M. 1999. Increasing flood risk and wetland losses due
748 to global sea-level rise: regional and global analyses. *Glob. Environ. Change* 9: S69–87

749 Olsen Associates Inc. (2012), Calibration of a Delft3D model for Bald Head Island and the Cape
750 Fear River entrance phase 1, 6114(April).

751 Orton, P., Georgas, N., Blumberg, A., and Pullen, J. (2012), Detailed modeling of recent severe
752 storm tides in estuaries of the New York City region, *J. Geophys. Res.*, 117, C09030,
753 doi:10.1029/2012JC008220.

754 Orton, P., Talke, S., Jay, D., Yin, L., Blumberg, A., Georgas, N., Zhao, H., Roberts, H.,
755 MacManus, K. (2015). Channel Shallowing as Mitigation of Coastal Flooding. *Journal of*
756 *Marine Science and Engineering*, 3(3), 654–673. <http://doi.org/10.3390/jmse3030654>

757 Orton, P. M., T. M. Hall, S. Talke, A. F. Blumberg, N. Georgas, and S. Vinogradov, 2016: A
758 validated tropical-extratropical flood hazard assessment for New York Harbor. *J. Geophys.*
759 *Res. Oceans*, 121, 8904–8929, doi:<https://doi.org/10.1002/2016JC011679>

760 [Pareja-Roman, L. F., Chant, R. J., & Sommerfield, C. K. \(2020\). Impact of historical channel
761 deepening on tidal hydraulics in the Delaware Estuary. *Journal of Geophysical Research:
762 Oceans*, 125, e2020JC016256. <https://doi.org/10.1029/2020JC016256>](#)

763

764 Parker, B. B., 1991. The relative importance of the various nonlinear mechanisms in a wide range
765 of tidal interactions. In: *Progress in Tidal Hydrodynamics*, Ed. by B. B. Parker, JohnWiley,
766 pp. 237-268.

767 Prandle, D., and Rahman, M. (1980). Tidal response in estuaries. *Journal of Physical*
768 *Oceanography*, 10(10), 1552–1573.

769 Ralston, D. K., Warner, J. C., Geyer, W. R., and Wall, G. R. (2013), Sediment transport due to
770 extreme events: The Hudson River estuary after tropical storms Irene and Lee, *Geophys.*
771 *Res. Lett.*, 40, 5451– 5455, doi:10.1002/2013GL057906.

772 Ralston, D. K., Talke, S., Geyer, W. R., Al-Zubaidi, H. A. M., & Sommerfield, C. K. (2019).
773 Bigger tides, less flooding: Effects of dredging on barotropic dynamics in a highly modified
774 estuary. *Journal of Geophysical Research: Oceans*, 124, 196–211.
775 <https://doi.org/10.1029/2018JC014313>

776 Savenije, H. H. G. (1998), Analytical expression for tidal damping in alluvial estuaries, *J Hydraul*
777 *Eng-Asce*, 124(6), 615–618.

778 Savenije, H. H. G., M. Toffolon, J. Haas, and E. J. M. Veling (2008), Analytical description of
779 tidal dynamics in convergent estuaries, *J. Geophys. Res.*, 113, C10025,
780 doi:10.1029/2007JC004408.

781 [Shen, J., & Gong, W. \(2009\). Influence of model domain size, wind directions and Ekman transport
782 on storm surge development inside the Chesapeake Bay: A case study of extratropical
783 cyclone Ernesto, 2006. *Journal of Marine Systems*, 75\(1-2\), 198–215.
784 <http://doi.org/10.1016/j.jmarsys.2008.09.001>](#)

785 [Shen, J., Wang, H., Sisson, M., & Gong, W. \(2006\). Storm tide simulation in the Chesapeake Bay
786 using an unstructured grid model. *Estuarine, Coastal and Shelf Science*, 68\(1\), 1–16.
787 <http://doi.org/10.1016/j.ecss.2005.12.018>](#)

788 Talke, S. A., P. Orton, and D. A. Jay (2014), Increasing storm tides in New York Harbor, 1844–
789 2013, *Geophys. Res. Lett.*, 41, 3149–3155, doi:10.1002/2014GL059574.

790 Talke, S. A., Familkhalili, R., & Jay, D. A. (2021). The influence of channel deepening on tides,
791 river discharge effects, and storm surge. *Journal of Geophysical Research: Oceans*, 126,
792 e2020JC016328. <https://doi.org/10.1029/2020JC016328>

793 Talke, S.A and D.A. Jay (2020). Changing tides: The role of natural and anthropogenic factors.
794 *Annual Review of Marine Science*, <https://doi.org/10.1146/annurev-marine-010419-010727>

795 Toffolon, M., and H. H. Savenije (2011), Revisiting linearized one-dimensional tidal propagation,
796 *J. Geophys. Res.*, 116, C07007, doi:10.1029/2010JC006616.

797 van Oldenborgh, G. J., van der Wiel, K., Sebastian, A., Singh, R., Arrighi, J., Otto, F., et al. (2017).
798 Attribution of extreme rainfall from Hurricane Harvey, August 2017. *Environmental*
799 *Research Letters*, 12, 124009

800 Wahl, T., S. Jain, J. Bender, S. D. Meyers, and M. E. Luther (2015), Increasing risk of compound
801 flooding from storm surge and rainfall for major US cities, *Nat. Clim. Change*, 5(12), 1093–
802 1097, doi:10.1038/NCLIMATE2736.

803 Wang, S.-Y. S., Zhao, L., Yoon, J.-H., Klotzbach, P., & Gillies, R. R. (2018). Attribution of climate
804 effects on Hurricane Harvey's extreme rainfall in Texas. *Environmental Research Letters*,
805 13. <https://doi.org/10.1088/1748-9326/aabb85>.

806 Winterwerp JC, Wang ZB, van Braeckel A, van Holland G, Kösters F. 2013. Man-induced regime
807 shifts in small estuaries—II: a comparison of rivers. *Ocean Dyn.* 63:1293–306

808 Wong, P. P., I. J. Losada, J.-P. Gattuso, J. Hinkel, A. Khattabi, K. L. McInnes, Y. Saito, and A.
809 Sallenger (2014), Coastal systems and low-lying areas, in *Climate Change 2014: Impacts,*
810 *Adaptation, and Vulnerability, Part A: Global and Sectoral Aspects, Contribution of*
811 *Working Group II to the Fifth Assessment Report of the Intergovernmental Panel on Climate*
812 *Change*, edited by C. B. Field et al., pp. 361–409, Cambridge Univ. Press, Cambridge, U. K.

813 Zheng, F.; Westra, S.; Leonard, M.; Sisson, S.A. Modeling dependence between extreme rainfall
814 and storm surge to estimate coastal flooding risk. *Water Resour. Res.* 2014, 50, 2050–2071.

815 Zscheischler, J., Westra, S., van den Hurk, B.J.J.M. et al. Future climate risk from compound
816 events. *Nature Clim Change* 8, 469–477 (2018). <https://doi.org/10.1038/s41558-018-0156-3>